remote sensing

MDPI

Article

Triggering of Land Subsidence in and Surrounding the Hangjiahu Plain Based on Interferometric Synthetic Aperture Radar Monitoring

Zixin He [1], Zimeng Yang [1], Xiaoyong Wu [2], Tingting Zhang [2], Mengning Song [1] and Ming Liu [1,*]

[1] Laboratory of Target Microwave Properties, Deqing Academy of Satellite Applications, Huzhou 313200, China; hzx@dasa.net.cn (Z.H.); yzm@dasa.net.cn (Z.Y.); smn@dasa.net.cn (M.S.)
[2] Aerospace Information Research Institute, Chinese Academy of Sciences, Beijing 100094, China; xywu@aircas.ac.cn (X.W.); zhangtt201832@aircas.ac.cn (T.Z.)
* Correspondence: euler@dasa.net.cn; Tel.: +86-151-0572-3809

Abstract: In the early stages, uncontrolled groundwater extraction led to the Hangjiahu (HJH) Plain becoming one of the areas with the most severe land subsidence in China. Since the beginning of this century, comprehensive measures have been taken to control the continuous aggravation of large land subsidence patterns in some areas; however, urban land subsidence issues, influenced by various factors, still persist and exhibit complex geographical distribution characteristics. In this study, we utilized Sentinel-1A images and the SBAS-InSAR technique to capture surface deformation over the HJH Plain in Zhejiang from 16 March 2017 to 20 January 2023. Through a comparative analysis with geological conditions, changes in surface mass loading, rainfall and groundwater, and land use types, we discussed the contributions of natural and anthropogenic factors to land subsidence. Augmented with optical remote sensing images and field investigations, we conducted a correlation analysis of the land subsidence status. The preliminary findings suggest that changes in surface mass loading and short-term heavy rainfall under extreme weather conditions can lead to periodic land subsidence changes in the region. Additionally, extensive infrastructure construction triggered by urbanization has resulted in significant and sustained land subsidence deformation. The research findings play an important guiding role in formulating scientifically effective strategies for land subsidence prevention and control, as well as urban planning and construction.

Keywords: Hangjiahu Plain; land subsidence; triggering; SBAS-InSAR; Sentinel-1A

Citation: He, Z.; Yang, Z.; Wu, X.; Zhang, T.; Song, M.; Liu, M. Triggering of Land Subsidence in and Surrounding the Hangjiahu Plain Based on Interferometric Synthetic Aperture Radar Monitoring. *Remote Sens.* **2024**, *16*, 1864. https://doi.org/10.3390/rs16111864

Academic Editors: Mozhdeh Shahbazi, Mohammad Omidalizarandi and Mohammad Ali Sharifi

Received: 25 April 2024
Revised: 15 May 2024
Accepted: 20 May 2024
Published: 23 May 2024

Copyright: © 2024 by the authors. Licensee MDPI, Basel, Switzerland. This article is an open access article distributed under the terms and conditions of the Creative Commons Attribution (CC BY) license (https://creativecommons.org/licenses/by/4.0/).

1. Introduction

Land subsidence, a geological hazard resulting from both geological and anthropogenic factors [1], presents a significant challenge globally. Presently, more than 150 cities across 60 countries and regions grapple with serious land subsidence issues [2,3], particularly in densely populated delta regions where it hampers socio-economic development and environmental conservation efforts [4,5], thus posing threats to human survival. Surveys project that by the end of this century, 11 low-lying coastal cities face inundation risks due to land subsidence [6], resulting in annual economic losses amounting to billions of dollars [7].

In China, nearly 100 cities, including those in the Yangtze River Delta [8–10], North China Plain [11,12], Fenwei Basin [13,14], and Pearl River Delta, are affected by land subsidence disasters [15,16], covering a total land subsidence area exceeding 79,000 km^2 [17]. Statistical analysis by Mehdi Bagheri-Gavkosh revealed that the eastern part of China's Yangtze River Delta registers among the regions with the highest average land subsidence values [18]. The Hangjiahu (HJH) Plain, situated in the southern part of the Yangtze River Delta, exemplifies land subsidence in this region.

The HJH Plain encompasses plains around cities, such as Hangzhou, Jiaxing, and Huzhou, with the maximum affected area reaching 4200 km^2 and a maximum cumulative land subsidence exceeding 100 cm [19]. Early studies suggested that excessive groundwater extraction was the primary trigger of land subsidence, resulting in aquifer and sediment layer compaction [20]. Since the beginning of this century, although governmental measures have been implemented to control the exacerbation of land subsidence in some areas [21], the continuous emergence of urban land subsidence funnels and cracks underscores the complexity of the causal mechanisms underlying land subsidence issues [22].

In recent years, with the rapid development of spaceborne SAR satellites [23,24] and SAR image processing technology [25], Interferometric Synthetic Aperture Radar (InSAR) technology has increasingly demonstrated its high-resolution, all-weather, and wide-coverage capabilities. These advantages have addressed the limitations of traditional geodetic techniques, which include low density, high cost, low timeliness, and weather constraints [26].Consequently, InSAR has become a crucial tool for monitoring land subsidence.

In the domain of land subsidence disaster monitoring, Differential InSAR (D-InSAR) has played a significant role in monitoring short-term, intense deformations [27,28]. For time-series monitoring, the most widely applied techniques are Persistent Scatterer InSAR (PS-InSAR) and Small Baseline Subset InSAR (SBAS-InSAR). PS-InSAR is a point-target analysis method [29,30], primarily used for detecting minute deformations in urban areas and critical infrastructure. To ensure the reliability of persistent scatterers, the continuous and regular acquisition of a sufficient number of images is necessary, enabling the high-precision displacement measurements of objects with stable scattering characteristics [31]. However, when the monitoring area is extensive and permanent scatterers are sparse, with widely distributed targets, PS-InSAR's effectiveness is limited. In contrast, SBAS-InSAR can provide better analysis in such scenarios [32]. Therefore, SBAS-InSAR is often employed in expansive natural environments, such as farmlands and mountainous regions. Unlike PS-InSAR, SBAS-InSAR does not focus solely on individual pixels but calculates based on the spatial distribution of coherence and mitigates coherence loss through small baseline subsets, thus requiring less stringent image conditions [31]. For complex and large-scale monitoring scenarios, combining both techniques can yield complementary benefits [33]. This approach not only meets the millimeter-level monitoring requirements over large areas but also detects changes in and the migration of land subsidence centers through time-series monitoring, revealing the overall distribution characteristics of regional land subsidence [34]. Unfortunately, despite the gradual establishment of a multi-technology coupled monitoring system in the HJH region since 2010 [35,36], as of 2023, the HJH Plain and its surrounding cities still have relatively few time-series InSAR monitoring results for land subsidence. These results are primarily based on monthly, quarterly, or even inter-annual analyses in the time domain, making it challenging to capture deformation characteristics over shorter periods and understand subtle processes of change [19,37–40].

This study employs the SBAS-InSAR technique and Sentinel-1A images to capture the surface deformation field in the Line-of-Sight (LOS) direction of the HJH Plain in Zhejiang Province from 16 March 2017 to 20 January 2023. The monitoring accuracy is assessed through cross-validation with PS-InSAR monitoring results. The study reveals the overall distribution characteristics of regional land subsidence and discusses the contributions of natural and anthropogenic factors through a comparison with geological conditions, changes in surface mass loading, rainfall and groundwater, and land use types. Additionally, correlation analysis, aided by optical remote-sensing images and field investigations, comprehensively elucidates the spatiotemporal characteristics of surface land subsidence in the HJH Plain and surrounding cities in Zhejiang Province. The research findings hold practical significance for formulating scientific strategies for land subsidence prevention and control and guiding urban planning and construction.

2. Geologic Setting

The HJH Plain is situated at the southern end of the Yangtze River Delta, bordered by Hangzhou Bay to the east, Qiantang River to the south, the eastern foothills of Mogan Mountain to the west, and extending north to Shanghai, Suzhou, and Lake Taihu, with a total area of approximately 6490 km² (Figure 1). Characterized as a Quaternary deposition area, the HJH Plain is predominantly covered by Quaternary deposits interspersed with occasional isolated hillocks and outcrops. The thickness of Quaternary deposits gradually increases from the southwest to the northeast, reaching a maximum thickness of nearly 300 m [41,42]. Influenced by neotectonics and marine transgression, the Quaternary strata in this region exhibit complex lithological facies, distinct sedimentary rhythms, and significant thickness variations. From bottom to top, the strata transition from continental deposits to river, lake, and deltaic coastal deposits [42,43]. The subsurface aquifer in this region is mainly composed of Quaternary alluvial gravel, gravel-bearing sand, and medium-fine sand. From top to bottom, it includes three aquifer units corresponding to the upper, middle, and lower Quaternary formations (Figure 2). The upper part of the aquifer is covered by cohesive soils of marine-lake facies, with interlayers of lacustrine and marine clay, forming a well-structured water-storage system [41]. The lower two aquifer units are primarily freshwater and represent the main exploited layers and important water sources in the region [41,43].

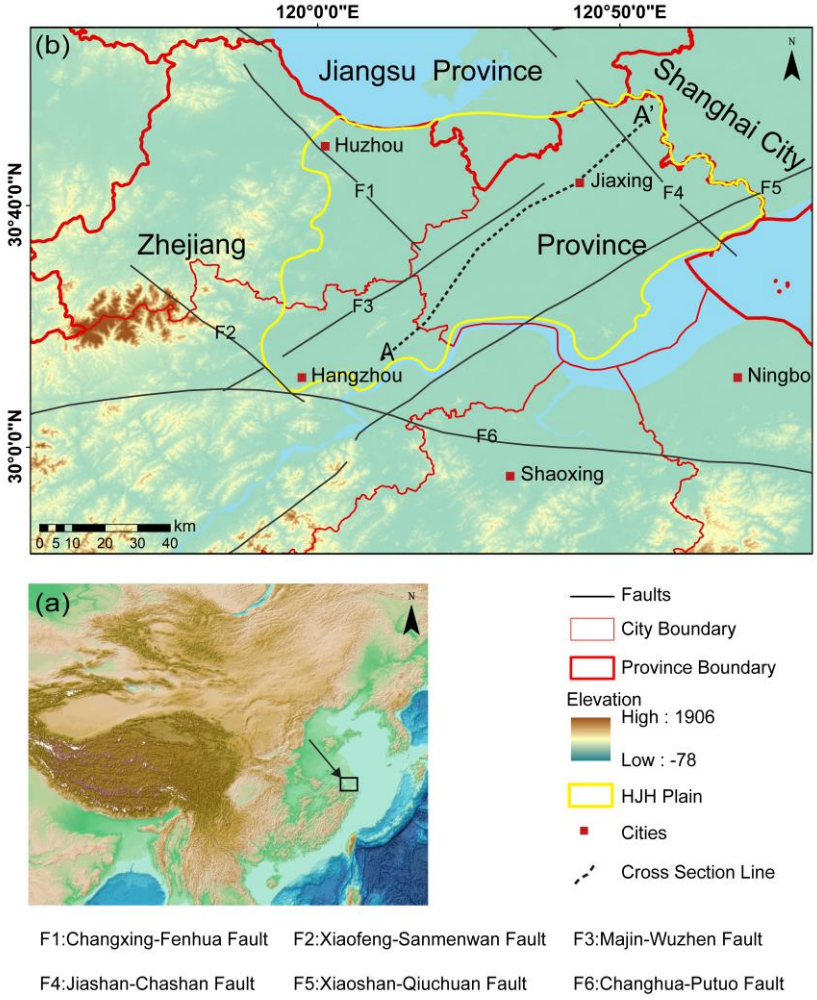

Figure 1. Study area location. (**a**) Geographical location of the study area; (**b**) Distribution of Hangjiahu (HJH) Plain and surrounding cities. The thick red line is the provincial boundary, the thin red line is the city boundary, the dotted line is the A–A′ section line, and the yellow line is the HJH Plain range.

Structurally, the HJH Plain is located on the eastern edge of the Yangtze Block. The region's fault structures exhibit characteristics of multi-periodicity and inheritance, with concealed faults and most covered by Quaternary loose sediments. The main manifestations include two sets of fractures trending northeast and northwest, with the northwest-trending faults forming later [44]. Notable faults influencing the HJH Plain include the Changxing-Fenghua Fault trending northwest and the Majin-Wuzhen Fault and Xiaoshan-Qiuchuan Fault both trending northeast (Figure 1b). Fault activity dating indicates that these three faults remained active during the late Pleistocene, with some activity extending into the Holocene [45–47], although their activity in the Holocene is relatively weak. Major engineering projects in the area need to consider the impact of fault activity and undergo a necessary comprehensive evaluation and analysis.

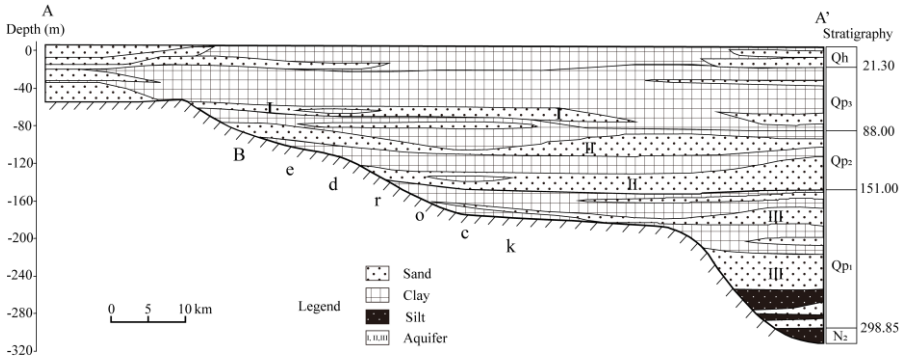

Figure 2. Hydrogeological cross-section of line A–A′ (principal strata of the underlying aquifer system in the HJH Plain).

3. Data and Method

3.1. Datasets

The Sentinel-1A, launched on 3 April 2014, is C-band radar satellite with a wavelength of approximately 5.55 cm. It operates with a repeat observation cycle of 12 days. The Interferometric Wide (IW) Swath mode employs Terrain Observation with Progressive Scans (TOPS) to acquire images consisting of three overlapping sub-swaths [48]. Each sub-swath contains 9 pulses in the azimuth direction, with black-fill borders in between. The spatial resolution is 5 m in the range direction and 20 m in the azimuth direction. The data can be freely acquired at https://search.asf.alaska.edu/ (accessed on 19 May 2024) [49,50]. The short repeat observation cycle and high resolution make Sentinel-1A a reliable data source for studying long-term deformation. We utilized 139 scenes of Single Look Complex (SLC) images from the IW mode, acquired along the ascending orbit (incidence angle of 39.66°) [51,52], covering the time span from 16 March 2017, to 20 January 2023, with a temporal interval of 12 days, except for some gaps (considering the impact of rapid vegetation growth during the summer months on coherence in the study area, we excluded some low-quality images from July, August, September, and October). The main parameters of the Synthetic Aperture Radar data used in this study are listed in Table 1.

Additionally, we obtained precise orbit data for Sentinel-1 from https://s1qc.asf.alaska.edu/aux_poeorb/ (accessed on 19 May 2024) to avoid errors in the baseline caused by inaccurate orbit information, which may manifest as residual stripes in interferograms [53]. We employed the fifth-generation atmospheric reanalysis model European Centre for Medium-Range Weather Forecasts (ECMWF) Reanalysis version 5 (ERA5) produced by the ECMWF to estimate tropospheric delay [54,55]. For assistance with registration, simulating terrain phases, removing flat ground phases, and geographic coding work, we employed 30 m resolution ASTER GDEM data [56]. Moreover, this study utilized geophysical fluid load products computed by the Earth System Model Group of the German Research Centre for Geosciences (ESMGFZ) [57] (http://rz-vm115.gfz-

potsdam.de:8080/repository), monthly precipitation data from the China National Meteorological Science Data Center (https://data.cma.cn/), water resources bulletin data released by the Water Resources Department of Zhejiang Province (https://slt.zj.gov.cn/col/col1229243017/index.html, accessed on 19 May 2024), and historical imagery data from Google Earth for an auxiliary analysis of experimental monitoring results.

Table 1. Main parameters of the Sentinel-1 SAR data used.

Parameter	Value
Band	C
Wavelength [52]	~5.55
Incidence angle(°)	39.66
Path/Frame	69/94
Direction	Ascending
Sensor mode	IW
Polarization	VV
Time span	16 March 2017–20 January 2023
Number of images	139

3.2. Methodology

The SBAS is currently one of the representative time-series InSAR methods [58–60]. This approach generates interferograms by selecting SAR images characterized by smaller spatial and temporal baselines, maximizing the utilization of images while mitigating decorrelation phenomena [61].

We employed the Stripmap Stack Processor of the InSAR Scientific Computing Environment (ISCE) 2.0 software for SBAS-InSAR interferogram processing [62]. The workflow is illustrated in Figure 3. First, the pulse overlaps of all slave acquisitions were extracted, and the geometric offsets between the slave burst overlaps and the stack master burst overlaps were roughly estimated. Then, the slave burst overlaps were resampled to the stack master burst overlaps, completing the coarse co-registration and generating differential overlap interferograms. Next, the Enhanced Spectral Diversity method (ESD) [63] was used to estimate the azimuth misregistration time series of all slave acquisitions relative to the stack master, and the range misregistration time series was estimated using amplitude correlation. The time series is a least-squares estimation derived from the pair misregistration from the previous step. Finally, by combining precise orbital data and external DEM, the geometric offsets between all slave SLCs and the stack master were calculated, and all bursts were merged to complete the fine co-registration of each burst SLC. Notably, In the temporal domain, each SAR image was paired with its three nearest neighboring images, resulting in 408 pairs of interferograms. Recognizing the trade-off between resolution and coherence in large-scale monitoring, we applied a multi-look processing with parameters of 9 in the azimuth direction and 27 in the range direction for each interferogram. Additionally, a Goldstein filter with an intensity threshold of 0.5 was used to filter the phase, and the Minimum Cost Flow (MCF) method was employed for phase unwrapping of interferograms [64].

We use the Advanced Rapid Imaging and Analysis [60] tools package suite [60] to prepare interferograms for time-series analysis in the Miami INsar Time series software in Python language (MintPy 1.5.1) [65]. Network optimization was performed based on a coherence threshold (0.7) and the Minimum Spanning Tree (MST) method, resulting in the removal of low-coherence pairs, leaving 81 remaining interferogram pairs. The remaining interferogram network was then inverted into a time-series phase using a Weighted Least Squares (WLS) approach [66]. For atmospheric corrections, we removed stratified tropospheric delays using the ERA5 weather reanalysis dataset [67] with PyAPS 3 software [68]. Noisy acquisitions are identified based on the residual phase root mean

squares, exceeding a predefined cutoff value of 3 times the median absolute deviations, and were subsequently excluded during the estimation of topographic residuals and average velocity [65].

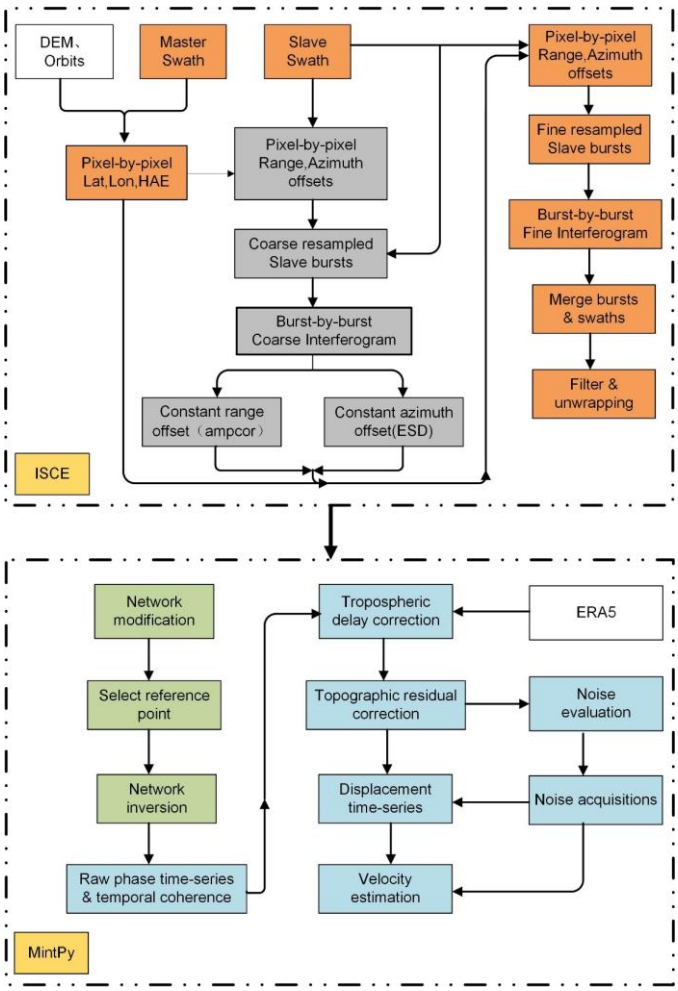

Figure 3. Workflow of Small Baseline Subset Interferometric Synthetic Aperture Radar (SBAS-InSAR) analysis. Orange block: full burst; grey block: overlap regions; green block: interferogram generation step; blue block: time-series deformation inversion step; white block: external input data.

In addition, we employed the PS-InSAR method on the dataset using SARscape 5.2.1 software [31]. This method focused on the deformation inversion of stable interferometric points (PS points) over the time series within the urban areas. Therefore, we selected the largest urban agglomerations in the study area, specifically Gongshu District and Xiaoshan District in Hangzhou, as the Control Experimental Area (CE Area). The inversion results were utilized to assess the accuracy of the SBAS-InSAR monitoring outcomes.

4. Results

4.1. Distribution of Land Subsidence

During the period spanning from 16 March 2017 to 20 January 2023, the average land subsidence rates along the LOS direction are depicted in Figure 4. Unlike traditional measurements that provide scattered point deformations, this study has captured deformation information covering over 80% of the study area. The findings reveal that the HJH Plain exhibits widespread stability with localized land subsidence. Land subsidence areas are dispersed across Hangzhou, Huzhou, Jiaxing, and Suzhou. Among these areas, Huzhou city exhibits the largest deformation area, whereas Jiaxing city shows the most stable land subsidence, with land subsidence rates in the plain primarily ranging from 1 cm/y to 3

cm/y. Land subsidence in the surrounding cities of the HJH Plain is primarily concentrated along the Qiantang River, with Shaoxing and Ningbo cities experiencing the most severe land subsidence, where land subsidence rates mostly range from 4 cm/y to 5 cm/y.

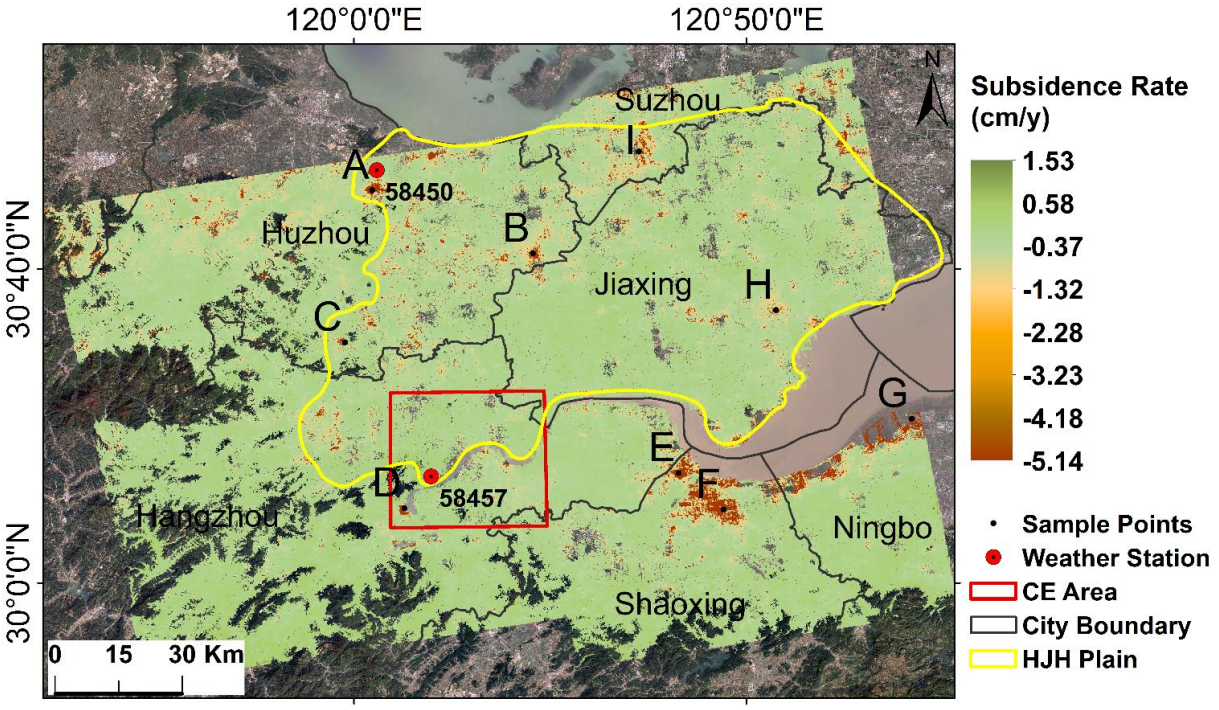

Figure 4. Line−of−sight (LOS) deformation rate of HJH plain and surrounding cities. Here, positive LOS velocities (in green) denote movement towards the satellite (e.g., uplift), while negative LOS velocities (in red) signify movement away from the satellite (e.g., subsidence). The red box is the Control Experimental Area (CE Area) of the two InSAR technology comparison experiments. A–I represent sample points located in key land subsidence areas. The two points with values 58,450 and 58,457 are weather stations and are used for the Section 5 in Section 5.1.3.

4.2. Time Series of Land Subsidence

Figure 5 presents the time-series information of cumulative surface land subsidence in the HJH Plain and surrounding cities from 26 March 2017 to 20 January 2023. Using the Sentinel-1A TOPS SAR image acquired on 16 March 2017, as the reference time for this time series, cumulative deformation values are recorded approximately once a year. Throughout this period, we observe a continual expansion of the overall area experiencing land subsidence deformation in the HJH Plain and surrounding cities, accompanied by a deepening trend in the degree of land subsidence deformation. However, there are also instances of slowdown and uplift of land subsidence deformation in certain areas, such as in the eastern part of Jiaxing city during 2021–2022 and in the eastern part of Huzhou city during 2022–2023.

To further explore the extent of surface deformation and the temporal characteristics of time-series changes in key land subsidence areas, we selected nine sampling points in regions displaying significant land subsidence for a detailed analysis. These sampling points include three in Huzhou, one in Hangzhou, two in Shaoxing, one in Ningbo, one in Jiaxing, and one in Suzhou. The deformation values throughout the time series, except for those corresponding to the dates of images excluded due to low coherence, were logged every 12 days and visualized in Figure 6.

Our analysis revealed that, apart from the trend of continuous land subsidence, each sampling point exhibits periodic deformation patterns. Specifically, deformation remains relatively small from November to the following May, while it intensifies from June to October, indicating significant short-term uplift and land subsidence phenomena. The

maximum deformation difference observed is 14 cm (at sampling point C, between 10 August 2021 and 3 September 2021).

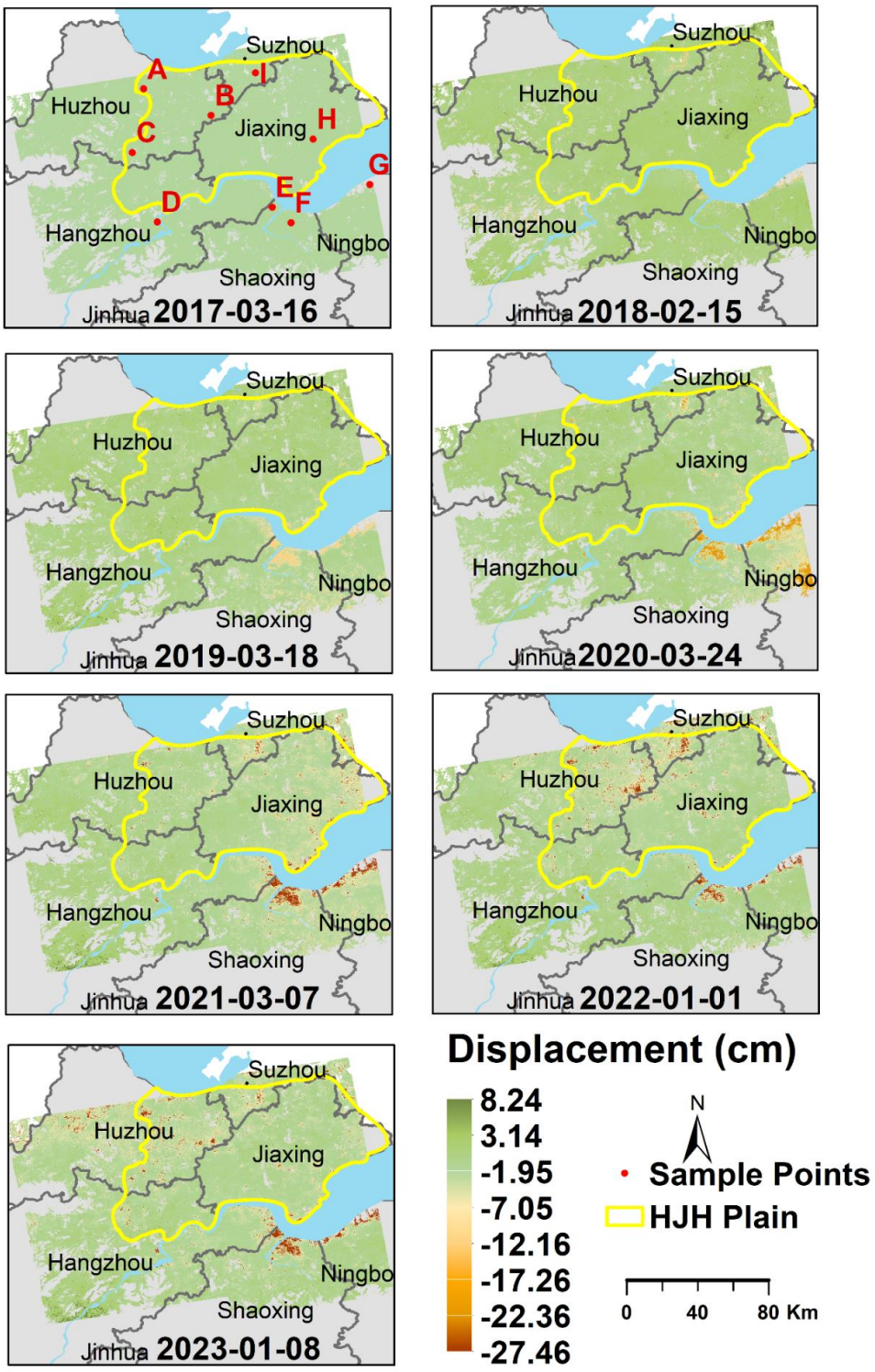

Figure 5. Time−series surface cumulative land subsidence in HJH plain and surrounding cities. A–I represent sample points located in key land subsidence areas.

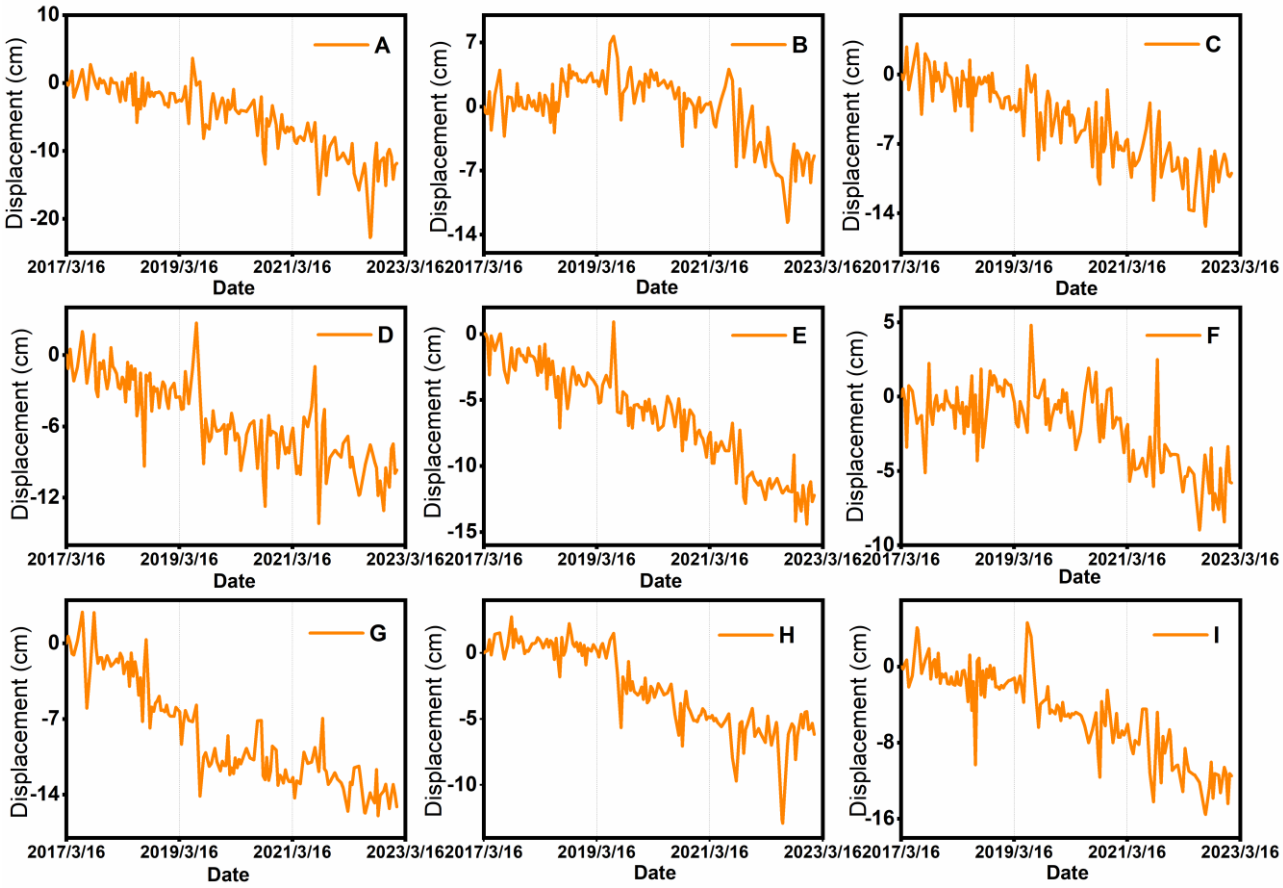

Figure 6. Time−series deformation curve of each settlement sampling point. (**A**–**I**) represent sample points located in key land subsidence areas.

4.3. Precision Checking

To assess the accuracy of the experimental results, we conducted a comparative experiment using PS-InSAR technology. Considering the limitations imposed by the widespread distribution of scattering bodies in the study area on the application of PS-InSAR, we selected the largest urban cluster in in the study area (Gongshu District and Xiaoshan District in Hangzhou City) as the CE Area, as outlined by the red box in Figure 4, for a simultaneous deformation assessment using the PS-InSAR method. The comparative results of the two methods are illustrated in Figure 7. Simultaneously, within the CE Area, we selected 25 point values (CE points) for cross-validation of the deformation assessment results, as depicted in Figure 8. The deformation trends obtained using both methods are entirely consistent, with an average error of 0.02 cm.

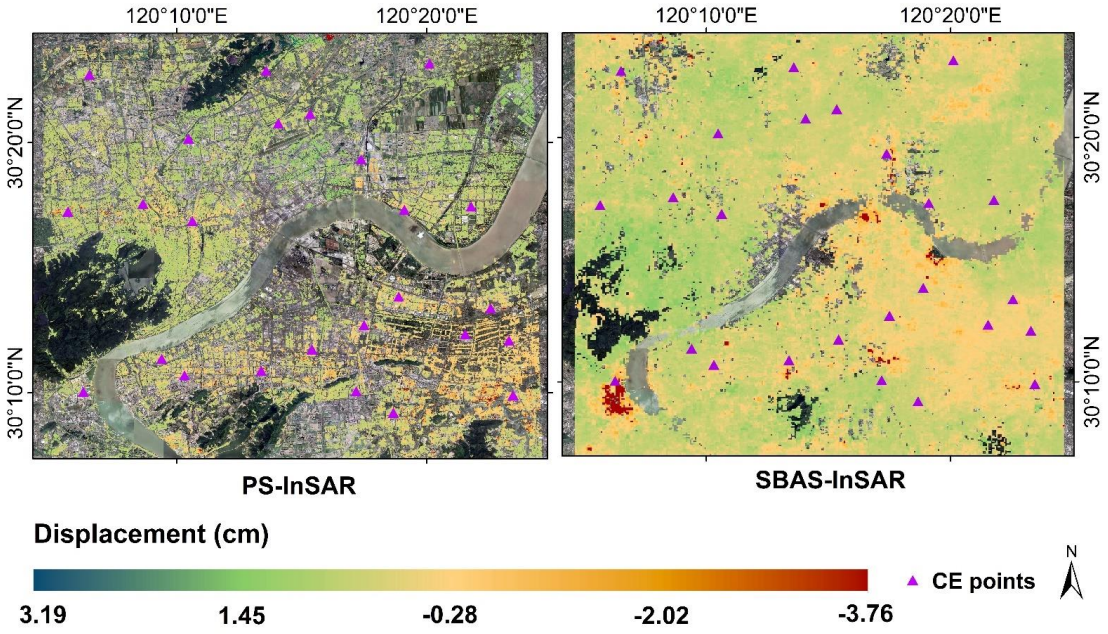

Figure 7. PS–InSAR and SBAS–InSAR cross-validation CE Area (Gongshu District and Xiaoshan District, Hangzhou City). There are 25 purple triangle points (CE points), which are used for the cross-validation of monitoring deformation accumulation between 16 March 2017 and 20 January 2023.

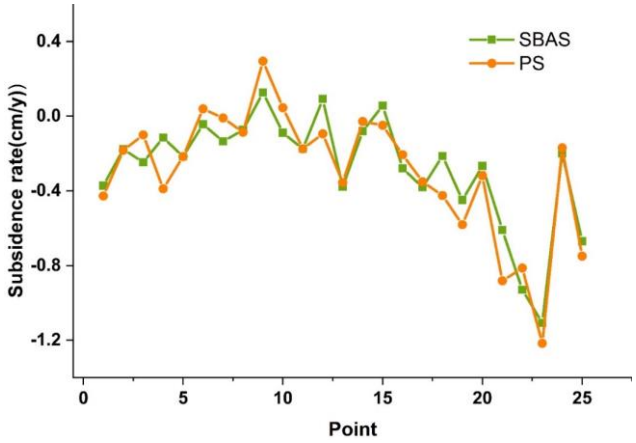

Figure 8. Result of PS–InSAR and SBAS–InSAR cross–validation.

5. Discussion

The prior research on land subsidence in this region primarily concentrated on groundwater extraction. Nonetheless, land subsidence has multifaceted origins, encompassing anthropogenic and natural factors, exhibiting temporal and regional variations. This study delves into the fundamental causes and mechanisms of land subsidence using InSAR-derived short-term deformation data, complemented by comprehensive data analysis. Certain monitoring outcomes may offer valuable insights for urban safety protocols and planning initiatives.

5.1. Natural Triggering of Land Subsidence

5.1.1. Neotectonic Movement

The HJH Plain and its neighboring areas in the late Quaternary generally retain characteristics of earlier tectonic movements, with relatively weak intensity of recent tectonic activity and low levels of fault activity. Two sets of faults with different orientations are

distributed in the study area. The NW-oriented faults are relatively active in later periods, and the overall crustal deformation in the region is characterized by low-rate differential uplift and land subsidence movements, accompanied by intermittent and oscillatory activities [69]. Roughly delineated by the Yixing-Huzhou-Hangzhou-Ningbo line, the southern part is in a state of extensive intermittent slow uplift, while the northern part, including the HJH Plain, experiences gradual land subsidence, with an average land subsidence rate ranging from 0.11 cm/y to 0.2 cm/y [44,70]. Compared to the current average land subsidence rate of 5.14 cm/y in the area, the contribution of recent tectonic movements to crustal deformation in this region is relatively weak.

5.1.2. Surface Mass Loading

In addition to surface deformation caused by neotectonic movement, attention has been directed towards crustal non-tectonic deformation resulting from changes in surface mass loading [71]. Such deformation was initially identified as systematic errors during the processing of GPS coordinate time-series changes [72]. Surface mass loading, leading to crustal non-tectonic deformation, primarily encompasses atmospheric loading, hydrological loading, and non-tidal ocean loading, in order to analyze the influence of surface mass loading on regional deformation.

We extracted the vertical deformation caused by surface mass loading at each land subsidence monitoring sampling point from the geophysical fluid load products of the German Research Center for Geosciences (ESMGFZ). The hydrological load product from ESMGFZ is based on the Land Surface Discharge Model (LSDM) [73], which models terrestrial surface hydrological processes, considering factors, such as snowmelt, seasonal glacier runoff, and river flow. These calculations are simulated according to the physics and parameterization of the Hydrological Discharge Model (HDM) and Simplified Land Surface Scheme (SLS). The atmospheric load and ocean load products combine data from the ECMWF, including atmospheric surface pressure, precipitation, evaporation, and temperature, and data from the Ocean Model for Circulation and Tides (OMCT) for non-tidal ocean bottom pressure. From these, the displacement of the Earth's surface due to load changes is calculated [57]. The accuracy and reliability of this data product have been confirmed through quality analyses involving various load models and GNSS data [74,75]. Figure 9 presents the time series information of load deformation at each land subsidence monitoring sampling point.

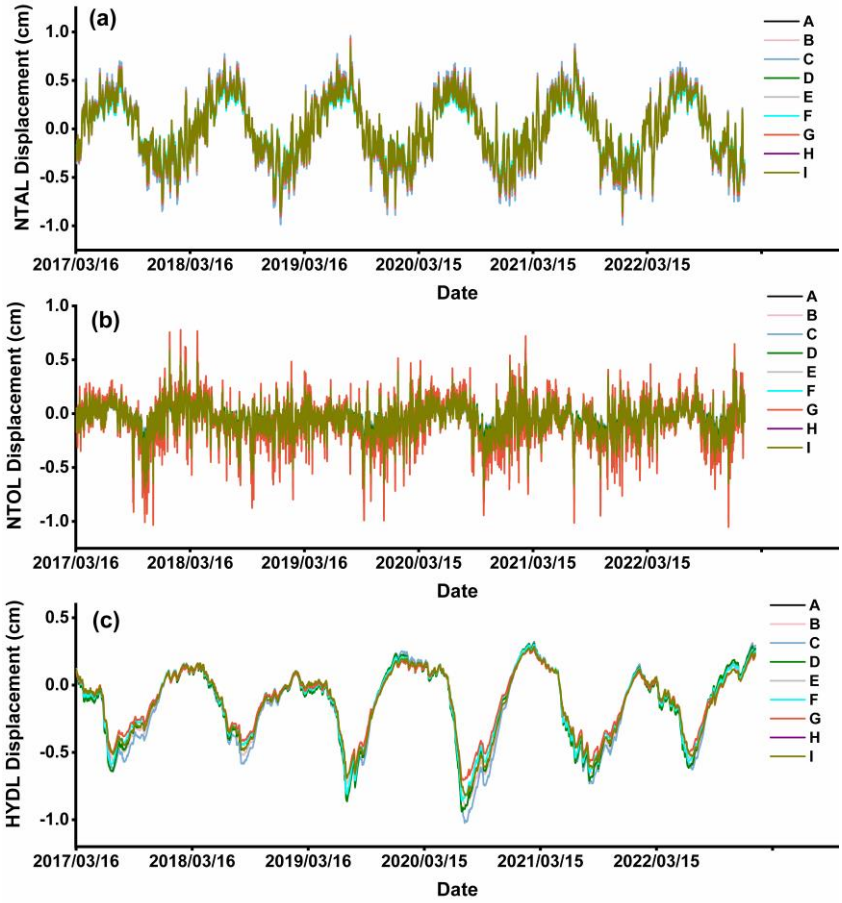

Figure 9. Time−series deformation of surface mass loading at deformation sampling points in each key land subsidence area. A−I represent sample points located in key land subsidence areas. A positive displacement represents vertical upward uplift deformation, and a negative displacement represents vertical downward land subsidence deformation. (**a**) Non−tidal atmospheric loading deformation, (**b**) non−tidal ocean loading deformation, (**c**) hydrological loading deformation. The time resolution of non−tidal atmospheric load deformation and non-tidal ocean deformation data is 3 h, and the time resolution of hydrological load deformation data is 24 h.

The study revealed that the time-series deformation of non-tidal atmospheric load and hydrological load at each point exhibited an inter-annual periodic elastic deformation pattern. Specifically, non-tidal atmospheric load deformation exhibited uplift from January to July and sinking from August to December, while hydrological load deformation showed sinking from January to July and uplift from the months August to December. The magnitude of settlement deformation remained relatively consistent, ranging between −0.7 cm and −0.8 cm. The magnitude of non-tidal atmospheric loading deformation is generally consistent across all points, which may be attributed to the similar latitude and elevation of the sampling points. Non-tidal ocean loading deformation is influenced by surface winds, atmospheric pressure changes, heat exchange, and humidity variations, leading to the migration of ocean water mass and changes in seabed pressure, thereby causing crustal deformation. Consequently, non-tidal ocean loading has a greater impact on coastal areas. For instance, at point G near the entrance of the Qiantang River into the sea in Ningbo City, the deformation value is significantly larger than at other points. In the HJH region, hydrological loading deformation is mainly controlled by the redistribution of land soil water and groundwater loads. The land subsidence values at sampling points in this area reach their maximum in July and August of each year, while the uplift values reach their maximum in February and March of the following year. This may be related to seasonal variations in the ocean, land, and monsoon.

As depicted in Figure 10, non-tidal atmospheric loading deformation contributes the most to land subsidence deformation, albeit within the range of −0.3 cm. Furthermore, the impact of hydrological loading deformation is characterized by uplift contributions, partially counteracting some of the land subsidence deformation. This suggests that surface mass loading deformation makes a relatively modest contribution to the overall land subsidence deformation.

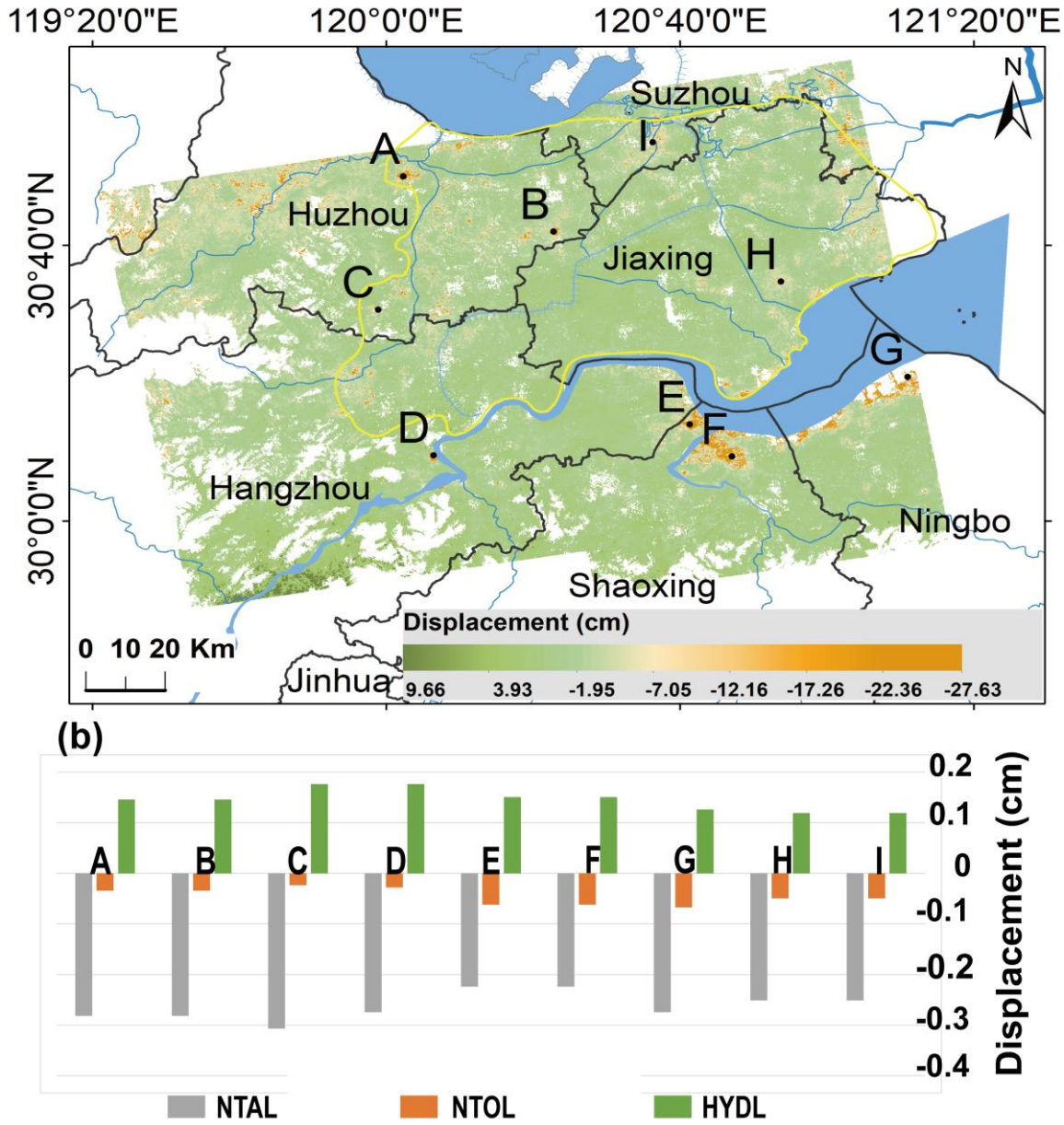

Figure 10. Cumulative surface deformation of the HJH Plain and surrounding cities from 16 March 2017 to 20 January 2023. A–I represent sample points located in key land subsidence areas. (**a**) Surface deformation monitored by SBAS-InSAR; (**b**) deformation caused by changes in surface mass loading.

5.1.3. Seasonal Rainfall

The short-term, dramatic uplift and land subsidence phenomena observed in the time-series deformation (Figure 6) exhibit clear seasonal variations, likely associated with extreme weather conditions and precipitation patterns. To investigate this correlation, we selected two land subsidence observation points, A and D, with prominent seasonal characteristics, and plotted the deformation from January 2021 to January 2023 (deformation

data missing for July 2022) in relation to monthly precipitation data obtained from nearby weather stations 58,450 and 58,457 (Figure 4).

Our analysis revealed that the impact of rainfall is related to changes in hydrological loading (hydrological loading deformation reaches its maximum land subsidence value in July and August each year and reaches its maximum uplift value in February and March of the following year) (Figure 9c). The year characterized by significant fluctuations in precipitation was particularly noticeable in 2021. During the months of June, July, and August 2021, both meteorological observation points experienced peak precipitation levels. Surface deformation during this period primarily manifested as uplift. Subsequently, from August to October, precipitation levels decreased, coinciding with significant land subsidence observations. By December, a noticeable uplift process resumed (Figure 11).

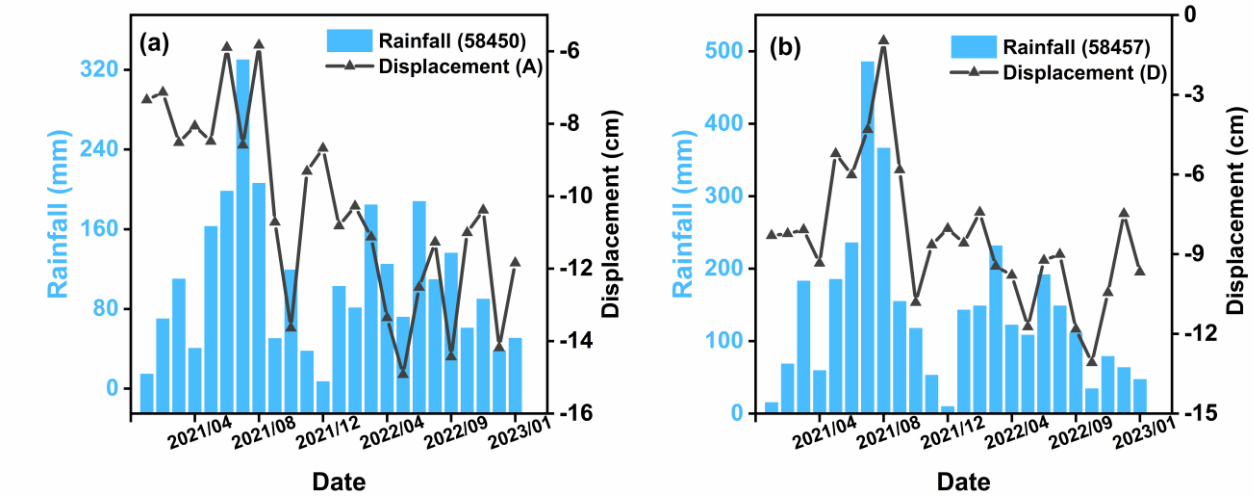

Figure 11. From January 2021 to January 2023, the rainfall changes at the two weather stations. (**a**) "58450" and the time series cumulative deformation changes at the corresponding sampling points A ; (**b**) "58457"and the time series cumulative deformation changes at the corresponding sampling points D.

This observed phenomenon can be attributed to the fact that June and July typically constitute the rainy season in the HJH region, marked by a substantial increase in rainfall. Increased soil moisture during this period leads to the expansion of soil particle interstitial spaces, resulting in surface uplift deformation. However, between August and October, frequent occurrences of typhoons and tropical storms often bring extreme weather conditions, such as strong winds and heavy rainfall, leading to localized flooding. The intense rainfall during this period erodes the softened soil post-rainy season, causing sediment loss and resulting in surface land subsidence deformation. The subsequent uplift observed may be attributed to precipitation replenishing groundwater through the water cycle, with deformation lagging behind precipitation on the time curve. This delayed response suggests a temporal lag between precipitation events and the subsequent effects on surface deformation.

5.2. Anthropogenic Triggering of Land Subsidence

Human socioeconomic activities, encompassing agriculture, industry, construction, and energy production, have significantly contributed to land subsidence. These activities induce changes in land use during urbanization, excavation, and landfill operations, altering the soil structure and compacting soil during agricultural processes. Additionally, underground resource extraction can lead to the formation of underground cavities, while the loss of original ground support exacerbates land subsidence phenomena.

In the early stages, the HJH Plain experienced severe land subsidence primarily due to excessive groundwater extraction. This resulted in the formation of numerous large

land subsidence centers, with the distribution closely aligned with water level funnels. Notably, Jiaxing City bore the brunt of these impacts, with maximum land subsidence displacements exceeding 80 cm [76]. These funnels are predominantly concentrated in urban areas of Jiaxing City, Tongxiang, Haiyan, and Pinghu (Figure 12). By analyzing groundwater extraction data from 2016 to 2022 (Figure 13), we observed that various local government restrictions on groundwater extraction, particularly stringent measures in Jiaxing City, have led to new changes in land subsidence patterns. In contrast to the previous clustering of land subsidence funnels, land subsidence has now transitioned to scattered patches (Figure 14), with most cumulative deformation values ranging from −1 cm to −5 cm. Presently, the most prominent areas of deformation are located in Huangwan Town, Haining County, along the Qiantang River coast, followed by Wuyuan Street in Haiyan County and Pinghu City. Through historical image analysis and field investigations of current land subsidence area land use, we infer that land subsidence in Huangwan Town, Haining County, may be linked to land reclamation and industrial construction activities, while land subsidence in Wuyuan Street, Haiyan County, and Pinghu City is associated with agricultural production activities.

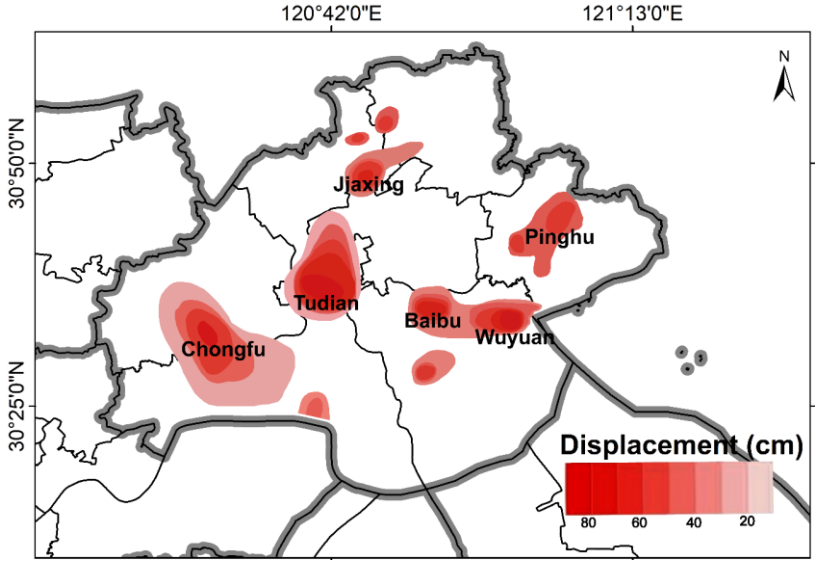

Figure 12. Distribution map of surface land subsidence funnels in Jiaxing City (1964–2018) (reference [76]).

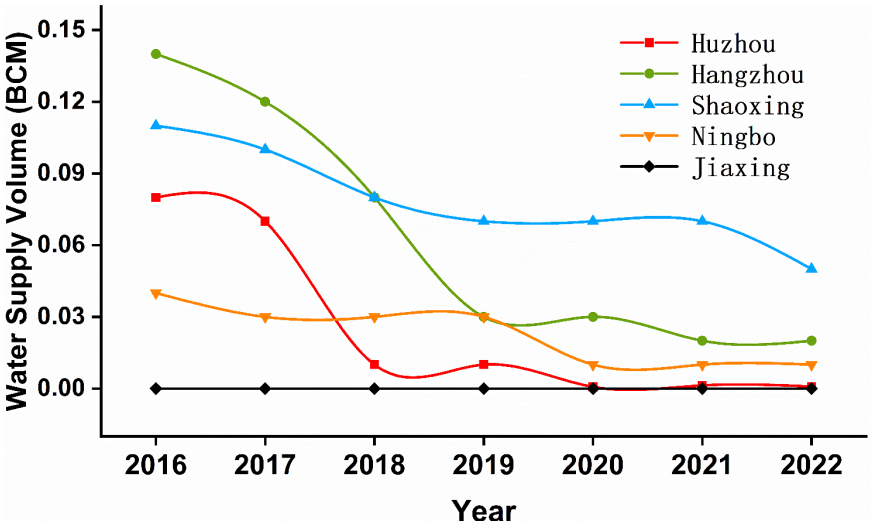

Figure 13. Groundwater extraction data in HJH Plain and surrounding cities from 2016 to 2022.

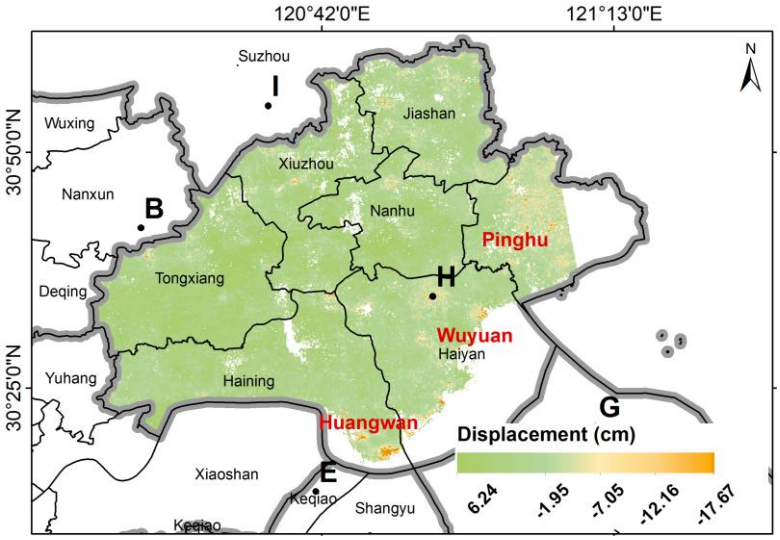

Figure 14. Surface land subsidence distribution in Jiaxing City from 16 March 2017 to 20 January 2023. "B,E,G,H,I" are sample points located in key land subsidence areas.

5.2.1. Agricultural Production

With continuous innovation in agricultural production technology, the expansion and transformation of agricultural land have emerged as significant contributors to land subsidence. Within the study area of this paper, including Nanxun District in Huzhou, Lin'an District in Hangzhou, Shangyu District in Shaoxing, Yuyao City in Ningbo, and Pinghu City in Jiaxing, these regions have long been predominantly agricultural areas. Deformation monitoring has unveiled widespread and uneven land subsidence, with Shangyu District in Shaoxing exhibiting the most severe land subsidence (Figure 15). Accumulated land subsidence values mostly range from −5 cm to −10 cm. Activities, such as agricultural irrigation, mechanized cultivation, and drainage system construction, may lead to the loss of soil support, increased soil density, and water loss, thereby exacerbating land subsidence issues. The non-uniformity of agricultural activities, differences in soil properties, and the utilization of water resources may contribute to the unevenness of land subsidence across the region.

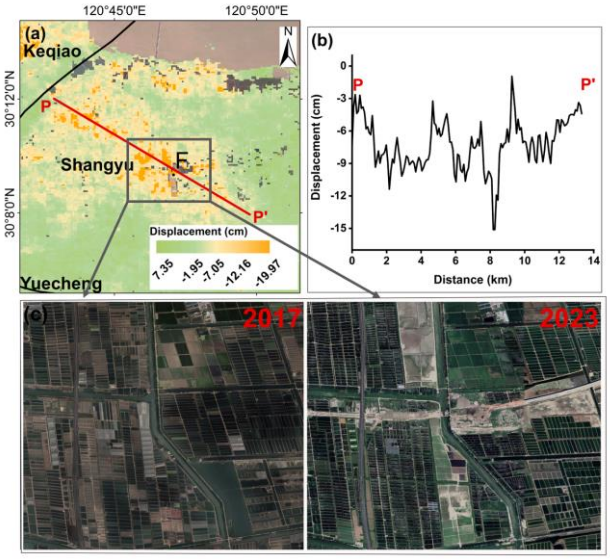

Figure 15. Typical land subsidence in Shangyu District, Shaoxing City. "F" is sample points located in key land subsidence areas. (**a**) Cumulative land subsidence from 16 March 2017 to 20 January 2023; (**b**) subsidence profile along PP'; (**c**) Google Earth images of the selected area in 2017 and 2023.

5.2.2. Engineering Construction

With the expansion of urban areas and the continual rise in high-rise buildings, land subsidence caused by transportation facilities, such as railways, bridges, and transportation loads, is becoming increasingly prevalent. Through land subsidence monitoring results, comparisons with historical imagery from Google Earth, and field investigations, several typical engineering construction cases were selected for a detailed analysis, including Deqing County in Huzhou, Xihu District in Hangzhou, and Cixi City in Ningbo.

The land subsidence areas of Deqing County and Xihu District exhibit similar patterns (Figures 16 and 17), characterized by distinct funnel shapes with clear boundaries. Notably, the land subsidence centers are situated in the southern part of Wukang Town in Deqing County and at the junction of Zhuantang Street and Shuangpu Town in Xihu District, with accumulated land subsidence ranging from approximately −11 cm to −13 cm. These areas have experienced continuous infrastructure construction, road paving, and drainage system installation activities from 2017 to 2023. Former farmland and bare land have been extensively developed, involving soil excavation and filling, which alter the physical and hydrological properties of the underground soil. Consequently, this weakens its bearing capacity, ultimately leading to land subsidence.

In newly constructed residential areas, monitoring and field investigations have unveiled significant cracks, serving as visible indicators of the impact of land subsidence on buildings. The emergence of cracks signifies that the land subsidence of the underground soil has reached a certain level, thereby adversely affecting the stability of building structures.

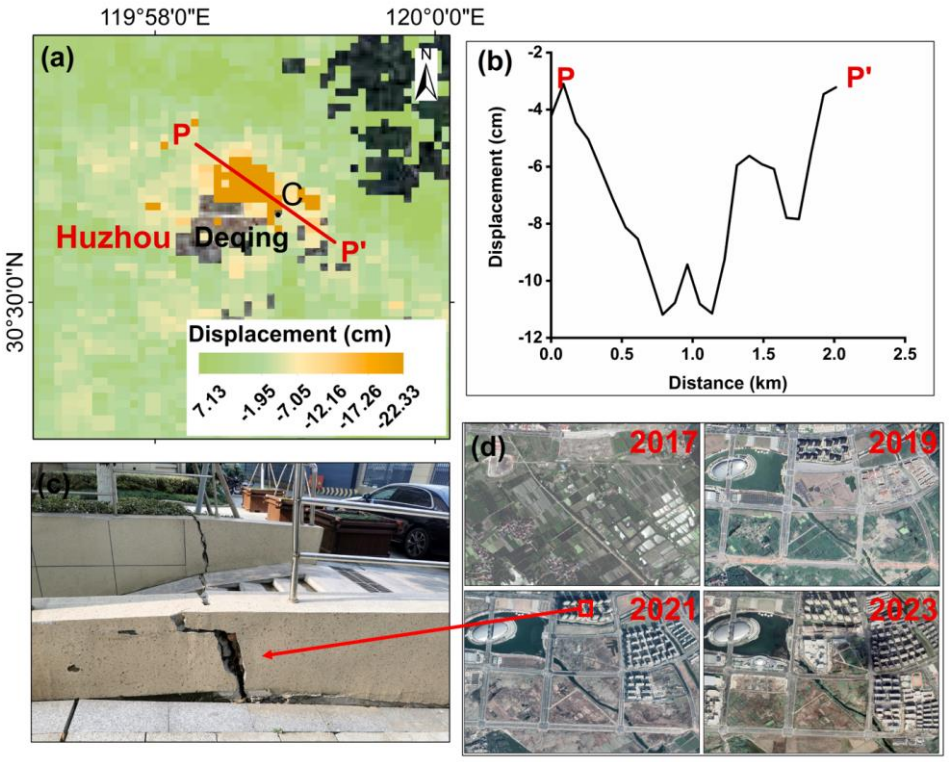

Figure 16. Typical land subsidence in Deqing County, Huzhou . "C" is sample points located in key land subsidence areas. (**a**) Cumulative land subsidence from 16 March 2017 to 20 January 2023; (**b**) subsidence profile along PP'; (**c**) cracks that have appeared in residential areas; (**d**) Google Earth images of the selected area in 2017–2023.

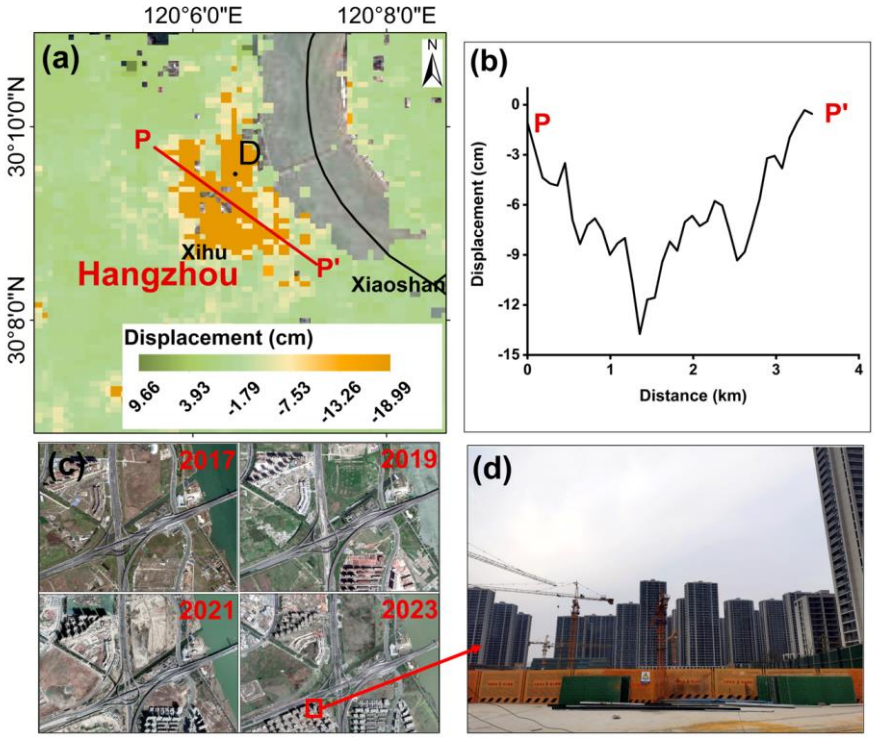

Figure 17. Typical land subsidence in Xihu District, Hangzhou. "D" is sample points located in key land subsidence areas. (**a**) cumulative land subsidence from 16 March 2017 to 20 January 2023; (**b**) subsidence profile along PP'; (**c**) Google Earth images of the selected area in 2017–2023; (**d**) actual ground construction conditions in selected areas.

A notable instance of land subsidence resulting from engineering construction in Ningbo City is situated at the Qiantang River estuary in Cixi City (Figure 18). Over the period from 2017 to 2023, there has been a complete transformation in land use within this area. In 2017, the entire expanse was dedicated to agriculture; however, by 2023, extensive urban residential buildings had replaced the agricultural landscape. The implementation of large-scale earthworks and excavation activities is expected to exert a significant impact on the underground soil structure and hydrological characteristics in this region. Of particular significance is the unique geographical location of the estuary area, characterized by soil predominantly composed of sediments brought by the river, such as silt and sand. These soils may exhibit relatively loose properties and strong sedimentation characteristics. The convergence of these factors has precipitated remarkably severe land subsidence phenomena. InSAR monitoring has further revealed substantial coherence loss within the area. According to the deformation results obtained, the maximum cumulative land subsidence in the region approximates −22 cm.

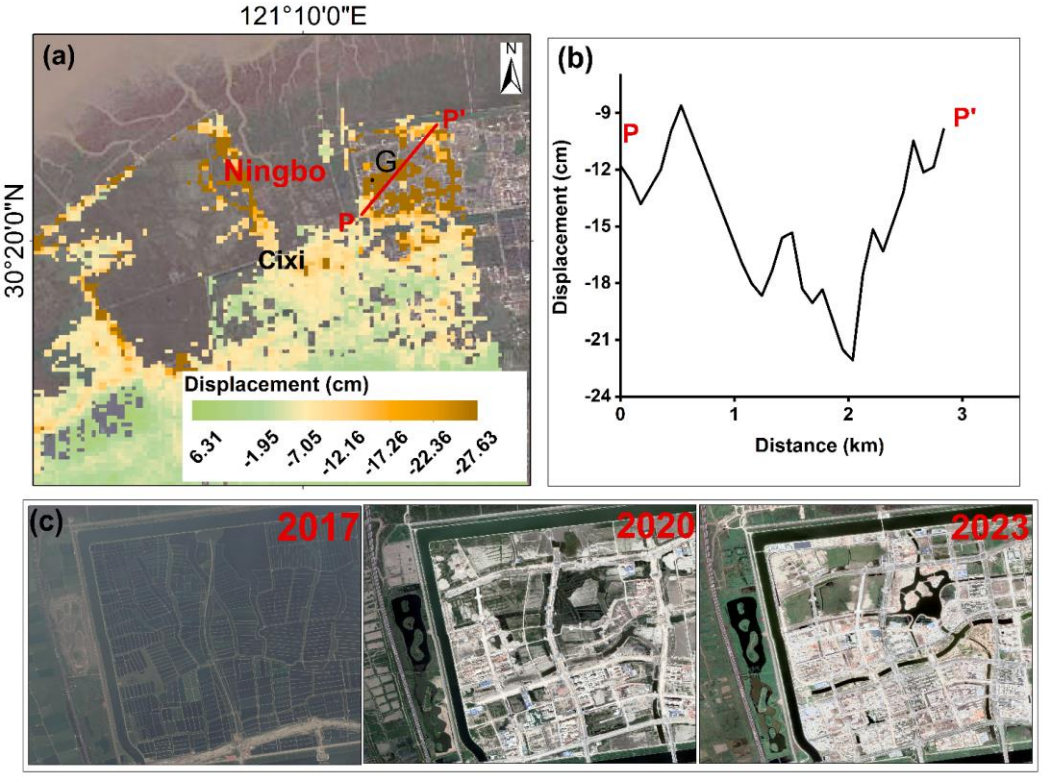

Figure 18. Typical land subsidence in Cixi City, Hangzhou. "G" is sample points located in key land subsidence areas. (**a**) cumulative land subsidence from 16 March 2017 to 20 January 2023; (**b**) subsidence profile along PP'; (**c**) Google Earth images of the selected area in 2017–2023.

6. Conclusions

In this study, we employed SBAS-InSAR monitoring technology and Sentinel-1A imagery to analyze ground deformation in the HJH Plain of Zhejiang Province and surrounding cities from 16 March 2017 to 20 January 2023, focusing on satellite LOS direction. The reliability of our monitoring approach was validated through cross-validation with PS-InSAR deformation fields. We have examined the diverse influences of both natural and anthropogenic factors on land subsidence, encompassing tectonic movements, alterations in surface mass loading, fluctuations in rainfall and groundwater levels, and industrial and agricultural practices. Our analysis was enriched by insights gleaned from optical remote sensing imagery and field investigations.

Our study revealed a notable shift in ground deformation patterns compared to the widespread land subsidence crisis witnessed in the HJH Plain prior to 2018. Presently, the deformation landscape displays widespread stability with localized land subsidence. Subsidence rates within the plain predominantly range between 1 and 3 cm/y, while in surrounding cities, particularly along the Qiantang River, such as in Shaoxing and Ningbo, most land subsidence rates range between 4 and 5 cm/y. We observed the progressive expansion in the geographical extent and deepening in the magnitude of land subsidence over time. Short-term abrupt uplift and land subsidence phenomena were primarily linked to seasonal rainfall patterns.

Human activities, notably agricultural production and engineering construction, emerged as the principal trigger of land subsidence. Key agricultural land subsidence areas include Nanxun District in Huzhou, Lin'an District in Hangzhou, Shangyu District in Shaoxing, Yuyao City in Ningbo, and Pinghu City in Jiaxing. Similarly, significant land subsidence due to engineering construction activities was identified in Deqing County in Huzhou, West Lake District in Hangzhou, and Cixi City in Ningbo. Notably, land subsidence stemming from industrial construction activities surpassed that arising from

agricultural production, with observed cracks in residential buildings posing potential risks to housing safety.

Author Contributions: Z.H. and M.L., methodology; Z.H., software; Z.H., validation; Z.Y. and M.S., formal analysis; Z.Y. and X.W., investigation; X.W., resources; Z.H. and M.L., data curation; Z.H. and M.L., writing—original draft preparation; M.L., writing—review and editing; Z.H. and M.L., visualization; M.L., supervision; M.L. and T.Z., project administration. All authors have read and agreed to the published version of the manuscript.

Funding: This research was supported by the Director Research Fund of Laboratory of Target Microwave Properties (No.2023-ZRJJ-001) and National Science Foundation of China, grant number 42071313. The APC was funded by the Director Research Fund of Laboratory of Target Microwave Properties.

Data Availability Statement: The original contributions presented in the study are included in the article, further inquiries can be directed to the corresponding author.

Acknowledgments: Thanks to Alaska Satellite Facility Data Search for organizing and providing the Sentinel-1A data download (https://search.asf.alaska.edu/#/, accessed on 19 May 2024), and acknowledgement for the data support from German Research Center for Geosciences (https://www.gfz-potsdam.de/en/, accessed on 19 May 2024).

Conflicts of Interest: The authors declare no conflicts of interest. The funders had no role in the design of the study; in the collection, analyses, or interpretation of data; in the writing of the manuscript; or in the decision to publish the results.

References

1. Galloway, D.L.; Burbey, T.J. Regional land subsidence accompanying groundwater extraction. *Hydrogeol. J.* **2011**, *19*, 1459.
2. Tongchun, Q.; Guoming, C.; Haigang, W. The latest progress of research on land subsidence abroad and its inspiration to China. *China Inst. Geo-Environ. Monit.* **2018**, *37*, 503–509.
3. Huang, B.; Shu, L.; Yang, Y. Groundwater overexploitation causing land subsidence: Hazard risk assessment using field observation and spatial modelling. *Water Resour. Manag.* **2012**, *26*, 4225–4239.
4. Schmidt, C. Alarm over a sinking delta. *Science* **2015**, *348*, 845–846.
5. Zhang, Y.; Si, Z.; Lin, X.; Zhang, Z.; Chu, H.; Cao, C.; Liu, Y.; Huang, H.; Huang, B.; Bai, Z. Time-series InSAR reveals new insights into land subsidence in the Yellow River Delta, China. *Mar. Georesour. Geotechnol.* **2024**, 1–10. https://doi.org/10.1080/1064119X.2024.2335678.
6. Bendarzsevszkij, A.; Eszterhai, V.; Gere, L.; Klemensits, P.; Polyák, E. World Economic Forum 2017. *Int. J. Res. Eng. Sci. Manag.* **2021**, *4*, 2.
7. Kok, S.; Costa, A.L. Framework for economic cost assessment of land subsidence. *Nat. Hazards* **2021**, *106*, 1931–1949.
8. Liu, Z.; Ng, A.H.-M.; Wang, H.; Chen, J.; Du, Z.; Ge, L. Land subsidence modeling and assessment in the West Pearl River Delta from combined InSAR time series, land use and geological data. *Int. J. Appl. Earth Obs. Geoinf.* **2023**, *118*, 103228.
9. Lu, Y.; Chen, D.; Chen, Y. Analysis of Spatiotemporal Land Subsidence Patterns of Suzhou City, China, over the Past 15 years Based on Multisource SAR Data. *J. Indian Soc. Remote Sens.* **2022**, *50*, 1347–1369.
10. Liu, C.; Shi, B.; Gu, K.; Zhang, T.; Tang, C.; Wang, Y.; Liu, S. Negative pore water pressure in aquitard enhances land subsidence: Field, laboratory, and numerical evidence. *Water Resour. Res.* **2022**, *58*, e2021WR030085.
11. Guo, H.; Zhang, Z.; Cheng, G.; Li, W.; Li, T.; Jiao, J.J. Groundwater-derived land subsidence in the North China Plain. *Environ. Earth Sci.* **2015**, *74*, 1415–1427.
12. Dong, J.; Guo, S.; Wang, N.; Zhang, L.; Ge, D.; Liao, M.; Gong, J. Tri-decadal evolution of land subsidence in the Beijing Plain revealed by multi-epoch satellite InSAR observations. *Remote Sens. Environ.* **2023**, *286*, 113446.
13. Ye, S.; Xue, Y.; Wu, J.; Yan, X.; Yu, J. Progression and mitigation of land subsidence in China. *Hydrogeol. J.* **2016**, *24*, 685.
14. Wang, F.; Peng, J.; Lu, Q.; Meng, Z.; Qiao, J.; Zang, M.; Zhao, J. Development characteristics and dynamic mechanisms of tectonic ground fissures in Weihe Basin, China. *Bull. Eng. Geol. Environ.* **2022**, *81*, 12.
15. Li, X.; Zhang, X.; Qiu, C.; Duan, Y.; Liu, S.a.; Chen, D.; Zhang, L.; Zhu, C. Rapid loss of tidal flats in the Yangtze River Delta since 1974. *Int. J. Environ. Res. Public Health* **2020**, *17*, 1636.
16. Yueping, Y.; Zuochen, Z.; Kaijun, Z. Land subsidence and countermeasures for its prevention in China. *Chin. J. Geol. Hazard Control* **2005**, *16*, 1–8.
17. Wu, J.; Shi, X.; Xue, Y.; Zhang, Y.; Wei, Z.; Yu, J. The development and control of the land subsidence in the Yangtze Delta, China. *Environ. Geol.* **2008**, *55*, 1725–1735.
18. Bagheri-Gavkosh, M.; Hosseini, S.M.; Ataie-Ashtiani, B.; Sohani, Y.; Ebrahimian, H.; Morovat, F.; Ashrafi, S. Land subsidence: A global challenge. *Sci. Total Environ.* **2021**, *778*, 146193.

19. Wu, H.; Zhang, Y.; Luo, G.; Mao, W.; Kang, Y.; Jin, Y. Ground subsidence monitoring over Jiaxing region, Zhejiang province from 2006 to 2010 using time series InSAR technique. *Int. Arch. Photogramm. Remote Sens. Spat. Inf. Sci.* **2015**, *40*, 181–184.
20. Jianyong, Y. The pain of sinking in the fertile wilderness. *Zhejiang Daily* **2005**, 33-0001.
21. Huizhen, S.; Jiankang, Z.; Sixiu, L.; Wei, L.; Mengjie, W.; Xiaoming, Z. The prevention of land subsidence on Hangjiahu plain. *Shanghai Land Resour.* **2014**, *35*, 114–117.
22. Zhou, L.; Wei, B.; Chen, G.; Liu, S.; Li, X.; Luo, Z.; Qin, D.; Zhang, D. InSAR time series analysis of natural and anthropogenic coastal plain subsidence: A case of Hangjiahu plain. *Geod. Geodyn.* **2024**. https://doi.org/10.1016/j.geog.2023.12.005.
23. Zhang, G.; Wang, S.; Chen, Z.; Zheng, Y.; Zhao, R.; Wang, T.; Zhu, Y.; Yuan, X.; Wu, W.; Chen, W. Development of China's spaceborne SAR satellite, processing strategy, and application: Take Gaofen-3 series as an example. *Geo-Spat. Inf. Sci.* **2024**, *27*, 221–236.
24. Euillades, J.A.; Roa, Y.L.; Euillades, L.D.; Euillades, P.A.; Rosell, P.A.; Solarte, E.A.; Perna, S. Interferometric Assessment of SAOCOM-1 TOPSAR Data. *IEEE Geosci. Remote Sens. Lett.* **2023**, *21*, 1–5.
25. Chang, S.; Deng, Y.; Zhang, Y.; Zhao, Q.; Wang, R.; Zhang, K. An advanced scheme for range ambiguity suppression of spaceborne SAR based on blind source separation. *IEEE Trans. Geosci. Remote Sens.* **2022,** *60*, 1-12.
26. Bokhari, R.; Shu, H.; Tariq, A.; Al-Ansari, N.; Guluzade, R.; Chen, T.; Jamil, A.; Aslam, M. Land subsidence analysis using synthetic aperture radar data. *Heliyon* **2023**, *9*, 3.
27. Peng, W.; Huang, X.; Wang, Z. Coseismic deformation and fault inversion of the 2017 Jiuzhaigou Ms 7.0 Earthquake: Constraints from steerable pyramid and InSAR observations. *Remote Sens.* **2022**, *15*, 222.
28. Liao, J.; Liang, C.; Wang, C.; Cao, F.; Ye, C.; Yang, Y. Source Model for the 2022 Qinghai Menyuan Ms 6.9 Earthquake Based on D-InSAR. *Front. Earth Sci.* **2022**, *10*, 948661.
29. Hussain, M.A.; Chen, Z.; Khan, J. Monitoring land subsidence in the Peshawar District, Pakistan, with a multi-track PS-InSAR technique. *Environ. Sci. Pollut. Res.* **2024**, *31*, 12271–12287.
30. i Bassols, J.B.; Declercq, P.-Y.; Vàzquez-Suñé, E.; Gerard, P. PS-InSAR data, key to understanding and quantifying the hydromechanical processes underlying the compaction of aquifer systems. Case of West-and East-Flanders, Belgium. *J. Hydrol.* **2023**, *624*, 129980.
31. Zhang, Z.; Hu, C.; Wu, Z.; Zhang, Z.; Yang, S.; Yang, W. Monitoring and analysis of ground subsidence in Shanghai based on PS-InSAR and SBAS-InSAR technologies. *Sci. Rep.* **2023**, *13*, 8031.
32. Bateson, L.; Novellino, A.; Hussain, E.; Arnhardt, R.; Nguyen, H.K. Urban development induced subsidence in deltaic environments: A case study in Hanoi, Vietnam. *Int. J. Appl. Earth Obs. Geoinf.* **2023**, *125*, 103585.
33. Zhang, P.; Guo, Z.; Guo, S.; Xia, J. Land subsidence monitoring method in regions of variable radar reflection characteristics by integrating PS-InSAR and SBAS-InSAR techniques. *Remote Sens.* **2022**, *14*, 3265.
34. Wang, S.; Sun, H.; Wei, L.; Pi, P.; Zeng, M.; Pan, Y.; Xue, Z.; Jiang, X. Integrated Assessment of Coastal Subsidence in Nansha District, Guangzhou City, China: Insights from SBAS-InSAR Monitoring and Risk Evaluation. *Remote Sens.* **2024**, *16*, 248.
35. Dong, S.; Samsonov, S.; Yin, H.; Ye, S.; Cao, Y. Time-series analysis of subsidence associated with rapid urbanization in Shanghai, China measured with SBAS InSAR method. *Environ. Earth Sci.* **2014**, *72*, 677–691.
36. Huang, Z.; Wang, F.; Xie, B.; Yu, L.; Zhang, D. Monitoring Land Subsidence by Using Multi-temporal Differential SAR Interferometry: A Use Case in Jiaxing, China. In Proceedings of the 2008 International Workshop on Education Technology and Training & 2008 International Workshop on Geoscience and Remote Sensing, Washington, DC, USA, 21–22 December 2008; Volume 1, pp. 591–595.
37. Zhang, Y.; Luo, G.; Mao, W.; Kang, Y.; Zhu, Y. Monitoring ground deformation in the Hangjiahu Plain using InSAR technique. In Proceedings of the MIPPR 2015: Remote Sensing Image Processing, Geographic Information Systems, and Other Applications, Enshi, China, 14 December 2015; Volume 9815, pp. 339–345.
38. Wu, H.; Zhang, Y.; Luo, G.; Kang, Y.; Zhu, Y. Monitoring Ground Subsidence in Areas Covered by Dense Vegetation Using Terrasar-X Images: A Case Study of Hangzhou. *Int. Arch. Photogramm. Remote Sens. Spat. Inf. Sci.* **2016**, *41*, 55–59.
39. Han, P.; Yang, X.; Bai, L.; Sun, Q. The monitoring and analysis of the coastal lowland subsidence in the southern Hangzhou Bay with an advanced time-series InSAR method. *Acta Oceanol. Sin.* **2017**, *36*, 110–118.
40. Wang, R.; Feng, Y.; Tong, X.; Li, P.; Wang, J.; Tang, P.; Tang, X.; Xi, M.; Zhou, Y. Large-Scale Surface Deformation Monitoring Using SBAS-InSAR and Intelligent Prediction in Typical Cities of Yangtze River Delta. *Remote Sens.* **2023**, *15*, 4942.
41. Jiankang, Z.; Mengjie, W.; Sixiu, L.; Huizhen, S. The Relation between Groundwater Exploitation and Land Subsidence in the Coast Plain of Zheiiang Province. *Geol. J. China Univ.* **2006**, *12*, 185–194.
42. Bai, L.; Yunbo, L.; Xiaowu, H. Implementation and Result Analysis of Level Monitoring of Land Subsidence in Hangiiahu Plain. *Zhejiang Brig. Surv. Mapp.* **2014**, *30*, 8–10.
43. Yun, J.; Jiankang, Z.; Chuan, Z. Analysis of land subsidence and groundwater resources development and utilization in Jiaxing City, Zhejiang Province. *Chin. J. Geol. Hazard Control* **1998**, *9*, 36–41.
44. Wei, Z. Crustal Deformation Monitoring and Mechanism Research in Hangzhou Area Based on D-InSAR. Ph.D. Thesis, Zhejiang University, Hangzhou, China, 2008.
45. Boyang, D.; Jiqing, Y.; Fanli, M.; Haibing, L. The tectonics around Hangzhou and the fault's influence on construction. *J. Zhejiang Univ. Technol.* **2003**, *31*, 319–323.
46. Qi, Y.; Wei, Z.; Lin, L.; Zhijiang, M.; Lifeng, M.; Xiang, G. Characteristics of Spatial Distribution and Activities of the Changxing-Fenghua Fault in Hangzhou Bay. *Geotecton. Et Metallog.* **2010**, *34*, 40–47.

47. Yanhui, M.; Wei, Z.; Jianyong, W. Application of Spatial Distribution of the Fault with Multi-resource Information -As an Example of Majin-Wuzhen Fault. *Bull. Sci. Technol.* **2013**, *29*, 110–113.
48. Zhang, Y.; Huang, H.; Liu, Y.; Bi, H.; Zhang, Z.; Wang, K.; Yan, L. Impacts of soft soil compaction and groundwater extraction on subsidence in the Yellow River Delta. *Mar. Georesour. Geotechnol.* **2021**, *39*, 1497–1504.
49. Qiao, X.; Chu, T.; Tissot, P.; Holland, S. Sentinel-1 InSAR-derived land subsidence assessment along the Texas Gulf Coast. *Int. J. Appl. Earth Obs. Geoinf.* **2023**, *125*, 103544.
50. García, A.J.; Bakon, M.; Martínez, R.; Marchamalo, M. Evolution of urban monitoring with radar interferometry in Madrid City: Performance of ERS-1/ERS-2, ENVISAT, COSMO-SkyMed, and Sentinel-1 products. *Int. J. Remote Sens.* **2018**, *39*, 2969–2990.
51. Zhou, H.; Wang, Y.; Yan, S.; Li, Y.; Liu, X.; Zhang, F. Monitoring of recent ground surface subsidence in the Cangzhou region by the use of the InSAR time-series technique with multi-orbit Sentinel-1 TOPS imagery. *Int. J. Remote Sens.* **2018**, *39*, 8113–8128.
52. Shankar, H.; Chauhan, P.; Singh, D.; Bhandari, R.; Bhatt, C.; Roy, A.; Kannaujiya, S.; Singh, R.P. Multi-temporal InSAR and Sentinel-1 for assessing land surface movement of Joshimath town, India. *Geomat. Nat. Hazards Risk* **2023**, *14*, 2253972.
53. Fernández, M.; Peter, H.; Arnold, D.; Duan, B.; Simons, W.; Wermuth, M.; Hackel, S.; Fernández, J.; Jäggi, A.; Hugentobler, U. Copernicus Sentinel–1 POD reprocessing campaign. *Adv. Space Res.* **2022**, *70*, 249–267.
54. Yu, C.; Li, Z.; Blewitt, G.J.E.; Science, S. Global comparisons of ERA5 and the operational HRES tropospheric delay and water vapor products with GPS and MODIS. *Earth Space Sci.* **2021**, *8*, e2020EA001417.
55. Dong, J.; Zhang, L.; Liao, M.; Gong, J. Improved correction of seasonal tropospheric delay in InSAR observations for landslide deformation monitoring. *Remote Sens. Environ.* **2019**, *233*, 111370.
56. Florinsky, I.; Skrypitsyna, T.; Luschikova, O. Comparative accuracy of the AW3D30 DSM, ASTER GDEM, and SRTM1 DEM: A case study on the Zaoksky testing ground, Central European Russia. *Remote Sens. Lett.* **2018**, *9*, 706–714.
57. Dill, R.; Dobslaw, H. Numerical simulations of global-scale high-resolution hydrological crustal deformations. *J. Geophys. Res. Solid Earth* **2013**, *118*, 5008–5017.
58. Dehghani Bidgoli, R.; Zandi Esfahan, E.; Pirasteh-Anosheh, H. An investigation of Earth surface deformation by SBAS-InSAR analysis. *Rend. Lincei Sci. Fis. E Nat.* **2024**, *35*, 213–221.
59. Xu, Y.; Fan, H.; Dang, L. Monitoring coal seam fires in Xinjiang using comprehensive thermal infrared and time series InSAR detection. *Int. J. Remote Sens.* **2021**, *42*, 2220–2245.
60. ArmaÅŸ, I.; Gheorghe, M.; Lendvai, A.M.; Dumitru, P.D.; BÄƒdescu, O.; CÄƒlin, A. InSAR validation based on GNSS measurements in Bucharest. *Int. J. Remote Sens.* **2016**, *37*, 5565–5580.
61. Tian, H.; Tao, Y.; Kou, P.; Alonso, A.; Luo, X.; Gong, C.; Fan, Y.; Lei, C.; Gou, Y. Monitoring and evaluation of gully erosion in China's largest loess tableland based on SBAS-InSAR. *Nat. Hazards* **2023**, *117*, 2435–2454.
62. Fattahi, H.; Simons, M.; Agram, P.; Sensing, R. InSAR time-series estimation of the ionospheric phase delay: An extension of the split range-spectrum technique. *IEEE Trans. Geosci. Remote Sens.* **2017**, *55*, 5984–5996.
63. Fattahi, H.; Agram, P.; Simons, M. A network-based enhanced spectral diversity approach for TOPS time-series analysis. *IEEE Trans. Geosci. Remote Sens.* **2016**, *55*, 777–786.
64. Chen, C.W.; Zebker, H.A. Two-dimensional phase unwrapping with use of statistical models for cost functions in nonlinear optimization. *J. Optim. Soc. Am. A* **2001**, *18*, 338–351.
65. Yunjun, Z.; Fattahi, H.; Amelung, F.J.C. Small baseline InSAR time series analysis: Unwrapping error correction and noise reduction. *Comput. Geosci.* **2019**, *133*, 104331.
66. Berardino, P.; Fornaro, G.; Lanari, R.; Sansosti, E. A new algorithm for surface deformation monitoring based on small baseline differential SAR interferograms. *IEEE Trans. Geosci. Remote Sens.* **2002**, *40*, 2375–2383.
67. Jolivet, R.; Grandin, R.; Lasserre, C.; Doin, M.P.; Peltzer, G. Systematic InSAR tropospheric phase delay corrections from global meteorological reanalysis data. *Geophys. Res. Lett.* **2011**, *38*. https://doi.org/10.1029/2011GL048757.
68. Jolivet, R.; Agram, P.S.; Lin, N.Y.; Simons, M.; Doin, M.P.; Peltzer, G.; Li, Z. Improving InSAR geodesy using global atmospheric models. *J. Geophys. Res. Solid Earth* **2014**, *119*, 2324–2341.
69. Jiageng, C.; Cunguo, C.; Li, W.; Bohui, L.; Yun, X. Earthquakes and neotectonic movements in Ningbo area. *Acta Seismol. Sin.* **1998**, *20*, 62–71.
70. Huiming, H.; Liren, H.; Guohua, Y. Modern crustal vertical movements in the Yangtze River Delta and adjacent areas. *Acta Geogr. Sin.* **1992**, *47*, 22–30.
71. Ke, D.; Xiaoying, G.; Wenqian, D.; Fuzong, C.; Wei, F.; Dingfa, H. Surface deformation characteristics of mass loading in the Sichuan-Xizang region. *Sci. Surv. Mapp.* **2023**, *48*, 28–42. https://doi.org/10.16251/j.cnki.1009-2307.2023.10.004.
72. Chuanzhen, S. Characteristics of Non-Tectonic Crustal Deformation from Surface Loads around ChineseMainland and Correction Model. Ph.D. Thesis, Institute of Geology, China Earthquake Administration, Beijing, China, 2013.
73. Dill, R. Hydrological Model LSDM for Operational Earth Rotation and Gravity Field Variations. 2008. Available online: https://gfzpublic.gfz-potsdam.de/pubman/faces/ViewItemOverviewPage.jsp?itemId=item_8770 (accessed on 19 May 2024).
74. He, Y.; Nie, G.; Wu, S.; Li, H. Comparative analysis of the correction effect of different environmental loading products on global GNSS coordinate time series. *Adv. Space Res.* **2022**, *70*, 3594–3613.
75. Glomsda, M.; Bloßfeld, M.; Seitz, M.; Angermann, D.; Seitz, F. Comparison of non-tidal loading data for application in a secular terrestrial reference frame. *Earth Planets Space* **2022**, *74*, 87.
76. Huang, J.; Xian, Y.; Li, W.; Zhang, D.; Zhuang, X.M. Hydrogeochemical evolution of groundwater flow system in the typical coastal plain: A case study of Hangjiahu plain. *Earth Sci.* **2021**, *46*, 2565–2582.

Disclaimer/Publisher's Note: The statements, opinions and data contained in all publications are solely those of the individual author(s) and contributor(s) and not of MDPI and/or the editor(s). MDPI and/or the editor(s) disclaim responsibility for any injury to people or property resulting from any ideas, methods, instructions or products referred to in the content.